ELSEVIER

Journal of Nuclear Materials 307–311 (2002) 171–178

journal of nuclear materials

www.elsevier.com/locate/jnucmat

Modeling the multiscale mechanics of flow localization-ductility loss in irradiation damaged bcc alloys

G.R. Odette [a,*], M.Y. He [a], E.G. Donahue [a], P. Spätig [b], T. Yamamoto [c]

[a] *Department of Mechanical and Environmental Engineering, University of California, Santa Barbara, CA 93106-5070, USA*
[b] *CRRP EPFL, Lausanne, Switzerland*
[c] *Tohoku University, Sendai 980-8579, Japan*

Abstract

Multiscale processes control the true [$\sigma(\varepsilon)$] and engineering [$s(e)$] stress–strain behavior of alloys. Strain hardening in unirradiated bcc alloys is modeled as a competition between production and annihilation of stored dislocations. Large increases in yield stress (σ_y) following irradiation are accompanied by loss of uniform engineering strain (e_u). All major features of the tensile test, including the effect of irradiation, can be modeled using finite element (FE) methods and a self-consistent $\sigma(\varepsilon)$ that differs markedly from $s(e)$. The irradiated $\sigma(\varepsilon)$ reflect large increases in σ_y and reductions in strain hardening. The very low tensile e_u following irradiation is due to enhanced continuum necking instabilities as a consequence of the intrinsic property changes. However, large elevations of $\sigma(\varepsilon)$ persist up to very high strains. Homogeneous deformation constitutive and plasticity theory can be used in continuum FE modeling of irradiated alloys. On a mesoscopic scale, FE simulations indicate that the irradiated $\sigma(\varepsilon)$ may be linked to an array of severely strain softening shear bands embedded in an irradiation hardened and strain hardening matrix.

1. Introduction

The ultimate objective of this work is to develop unified, physically-based models of deformation of bcc alloys for use in fusion reactor first wall and blanket structures. We focus here on the true stress–strain $\sigma(\varepsilon)$ constitutive behavior, typically characterized in tensile tests, outside both the creep and dynamic strain aging regimes. First we apply a simple phenomenological model of strain hardening in unirradiated alloys based on dislocation theory concepts. The mechanism based form proposed for the $\sigma(\varepsilon)$ law facilitates modeling its relation to the underlying material microstructure, as well as its use in finite element (FE) studies. Modeling the effects of irradiation initially focuses on the relation of the $\sigma(\varepsilon)$ to the engineering stress–strain $s(e)$ curve obtained from tensile tests. In particular, we seek to develop a framework for developing a multiscale understanding of post-yield strain hardening and the associated measures of tensile ductility. To this end, we also carry out FE simulations of heterogeneous deformation in materials with locally strain softening shear band regions embedded in a strain hardening matrix.

The phenomenological true stress–true strain model for unirradiated bcc alloys extends previous work on the strain rate (ε') and temperature (T) dependence of the yield stress, $\sigma_y(\varepsilon, \varepsilon', T)$ and more empirical descriptions of the substantial post-yield strain hardening in both ferritic–martensitic steels and vanadium alloys. Details of the work are summarized elsewhere and only the most salient results are summarized below [1–3].

Intermediate temperature irradiation to a few dpa results in significant radiation hardening and severe loss of uniform *engineering* strain (e_u) capacity (e.g., see Refs. [4–7]). Note, we use e_u to emphasize that it is a measure specific to the tensile test; however, e_u can be readily

* Corresponding author. Tel.: +1-805 893 3525; fax: +1-805 893 8651.
E-mail address: odette@engineering.ucsb.edu (G.R. Odette).

0022-3115/02/$ - see front matter
PII: S0022-3115(02)01136-4

related to the true uniform stain through the standard relation, $\varepsilon_u = \ln(1 + e_u)$. As discussed in Section 3, beyond the point of necking, the relationship between ε and e is much more complex. Fig. 1 shows a typical set of $s(e)$ curves in the unirradiated condition and following irradiation for the program heat of the V–4Cr–4Ti alloy irradiated to ≈0.4 dpa over a range of temperature [5]. The unirradiated $s(e)$ curve shows a typical Luder's-type behavior followed by significant strain hardening. The irradiated curves at 420 and 325 °C show the progressive effects of increasing σ_y and decreasing e_u, which approaches 1% or less as the temperature diminishes and is negligible at 270 and 110 °C. At low irradiation temperatures the $s(e)$ curves also show an apparent yield drop, followed by a more gradual decrease in load. Note these apparent yield drops are neither sudden nor followed by a lower yield stress plateau as is observed typically in alloys with so-called source hardening by dislocation atmospheres of interstitial solutes.

Ductility loss is accompanied by increasingly heterogeneous internal deformation patterns ranging from some coarsening of slip to formation of very localized and highly strained flow channels which have been predominantly studied in fcc metals and alloys [6–8]. It is assumed that these phenomena are due to one or more of the following processes: (a) source hardening and unlocking of dislocations from atmospheres of cluster defects [6,7]; (b) destruction of pinning defects in strain softening in flow channels [7–11]; twinning [12]; and retardation of cross slip [13].

However, the role of flow localization in macroscopic ductility loss has not been established. Indeed, some degree of heterogeneous deformation is common even in materials with substantial e_u; and even the occurrence of channeling does not always result in low uniform strains. Indeed, we recently showed that the loss of uniform strain in a tensile test is dominated by the macroscopic onset of necking and can be rationalized without recourse to the occurrence of heterogeneous

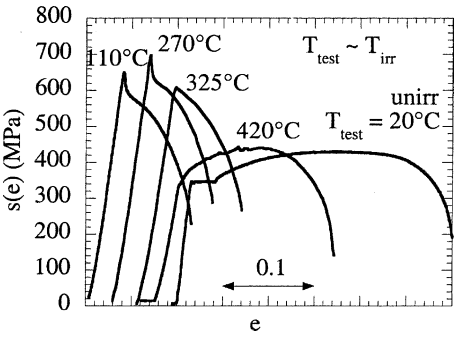

Fig. 1. Experimental load–displacement engineering stress–strain curves for a V–4Cr–4Ti alloy in the unirradiated and irradiated conditions (the curves are off-set for clarity and include the effects of load train compliance).

flow [14]. Thus to understand low e_u, it is necessary to make a clear and quantitative distinction between engineering $s(e)$ curves and the underlying *effective* true stress (σ)–*effective* plastic strain (ε) constitutive law, $\sigma(\varepsilon)$. In a tensile test, the relation between $s(e)$ and $\sigma(\varepsilon)$ can be established simply only up to the point of necking. Since the corresponding strain range is small to negligible in the irradiated materials of interest, great caution must be used in interpreting the macroscopic observables from a tensile test in terms of the basic microscopic material behavior.

We have previously derived a simple analytical model demonstrating that ε_u is controlled by both the yield stress (σ_y) and strain hardening, using a power law model as $\sigma(\varepsilon) = \sigma_y + \kappa_{sh}(\varepsilon/\varepsilon_y)^n$ [14]. The model shows that large increases in σ_y, coupled with reduced, but finite, $\kappa_{sh}(\varepsilon/\varepsilon_y)^n$ result in very low ε_u and e_u. Further, we have shown that *all the key features* of $s(e)$ curves, including the high ε region in the neck, can be reproduced by FE simulations of the tensile test based on standard continuum, homogeneous plasticity models. As summarized below, even in the most severe cases with $e_u \approx 0$ and an apparent yield drop, the engineering $s(e)$ are consistent with a $\sigma(\varepsilon)$ constitutive law characterized by a region of modest softening over an increment of a few percent of ε, followed by a strain hardening regime up to high ε. Notably, a large fraction of the irradiation hardening at yield ($\Delta\sigma_y$) also persists in the irradiated $\sigma(\varepsilon)$ up to high strains.

The key physical link between the macro and micro phenomena is the compatibility and equilibrium requirements of the *laws* of solid mechanics. Specifically, redistribution of stress and stress-state occur in any heterogeneously deforming material. These re-distributions are also influenced by the overall deformation pattern. For example, in a very thin specimen or a single crystal test, particularly when displacements normal to the tensile axis are relatively unconstrained, deformation may occur in only a single, or a few, dominant shear bands. In contrast, deformation in the interior grains of a polycrystalline alloy in a specimen with axial displacement constraint, requires multiple slip orientations. In this case, the compatibility requirement tends to homogenize deformation even in constitutively heterogeneous materials. Specifically, the effective deviatoric stresses in soft regions are reduced by local redistribution of loads to the adjoining harder regions as well as increases of the multiaxial mean stress. We address this issue in Section 4 using a composite cell model composed of strain softening shear bands embedded in a strain hardening matrix.

A key practical question is as follows: can continuum level descriptions of the macroscopic behavior that are relatively independent of the microscopic detail adequately describe macroscopic stress–strain (load–displacement) behavior in test specimens and structures

(and if so when)? From a more fundamental perspective, deformation is an inherently multiscale phenomena. Thus proper modeling the effects of the meso-scale and macro-scale processes is necessary for achieving real understanding of both the causes and consequences of the microscale phenomena, such as localization and channeling.

2. A dislocation theory-based unified constitutive model for bcc alloys

We begin with some background by describing the constitutive law as

$$\sigma(\varepsilon, \varepsilon', T) = \sigma_{yt}(\varepsilon', T) + \sigma_{ya} + \sigma_{sh}(\varepsilon, T). \quad (1)$$

Here, the thermally activated component of the yield stress, $\sigma_{yt}(\varepsilon', T)$, depends on both temperature and strain rate. This term is primarily controlled by the lattice Peierls stress and, to a lesser extent, by other processes such as short-ranged dislocation pinning sites including interstitial carbon and nitrogen. The second σ_{ya} term represents the athermal component of the yield stress that depends weakly on temperature, scaling with the elastic modulus. Dispersed obstacles to dislocation slip, as well as the grain and dislocation network-cell substructures control the magnitude of this term. Interstitial solute and possibly irradiation defect atmospheres segregated to the dislocation strain fields may also add to σ_{ya}. Both the $\sigma_{yt}(\varepsilon', T)$ and σ_{ya} terms where characterized in previous studies of both unirradiated martensitic steels and V–4Cr–4Ti alloys [1–3] and they are more generally the subject of a very large historical literature; hence, they will not be discussed further in this paper. The third term $\sigma_{sh}(\varepsilon, T)$ represents the alloy strain hardening behavior. In contrast to the typical power law representation of strain hardening ($\sigma \propto \varepsilon^n$), the Zerelli–Armstrong representation [15] provides a proper basis to decompose the physics that control initial yielding from the processes mediating subsequent strain hardening. For example, strain hardening is typically much less sensitive to temperature than σ_y, and primarily depends on the combination of coarse phase, grain and subgrain structures that control dislocation evolution as a function of plastic strain. Note the present study does not attempt to deal with strain rate or temperature dependent dynamic strain aging, leading to additional hardening and serrated flow curves at finite plastic strains [5].

The strain hardening model is based on competing dislocation storage and annihilation processes [16,17]. Plastic strain (ε) creates new dislocations with a total density, ρ, in the form of network and sub-cell structures, at a rate $d\rho^+/d\varepsilon$ as primarily controlled by a characteristic slip length. The slip length is on the order of a characteristic 'grain' dimension, D_c, believed to be approximately the lath size in martensitic steels. Dislocations are annihilated at a rate $d\rho^-/d\varepsilon$ proportional to the net stored dislocation density, ρ. Strain hardening increases with $\sqrt{\rho}$ up to saturation where $d\rho^+/d\varepsilon = d\rho^-/d\varepsilon$.

The simple model was used to fit the strain hardening data in three martensitic steels. The characteristic $D_c \approx 3$–10 μm is on the order of the lath size, but may be slightly temperature dependent. The values of D_c are roughly similar in the three steels, but is largest in a F82H and smallest in a JLF-1. The annihilation rate parameter is also similar in all three cases, but again is slightly larger in F82H and slightly smaller in JLF-1. The $d\rho^-/d\varepsilon$ increases approximately linearly with temperature, reflecting reduced dislocation mobility, from ≈ 0 at 100 K to a very high of level $\approx 90\rho$ at 700 K.

Fig. 2(a) shows the $\sigma_{sh}(\varepsilon, T)$ for Eurofer 97 over a wide range of temperature. Fig. 2(b) shows the corresponding curves at 298 K for the three FM steels that exhibit generally similar behavior. Note the nominal

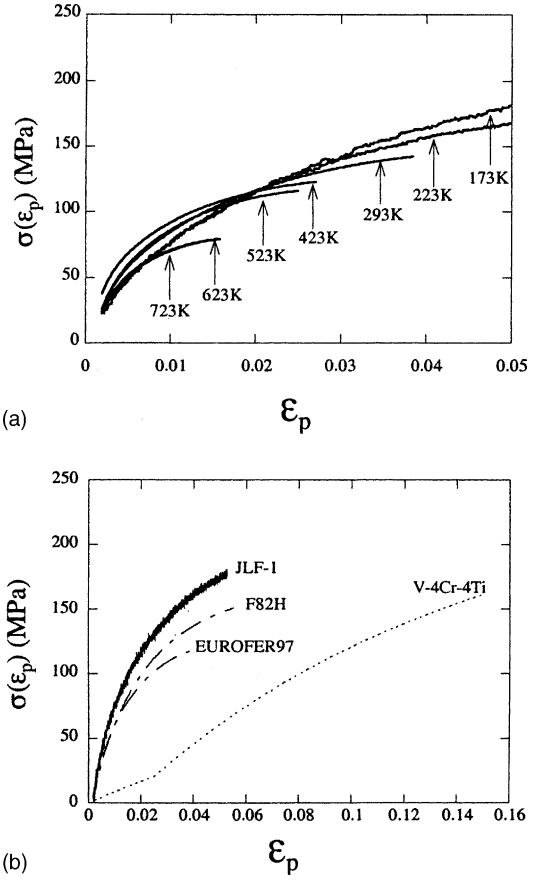

Fig. 2. (a) $\sigma_{sh}(\varepsilon, T)$ for Eurofer 97 over a wide range of temperatures; (b) $\sigma_{sh}(\varepsilon, T)$ at 298 K for the three martensitic steels and a V–4Cr–4Ti alloy.

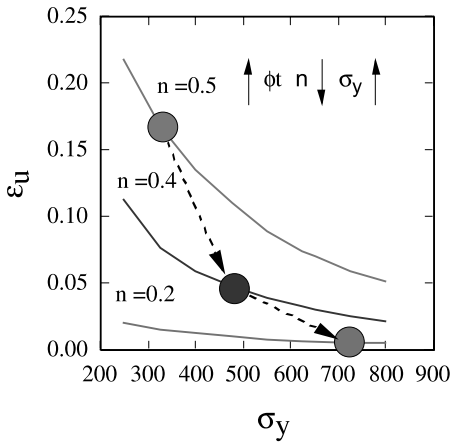

Fig. 3. Variation of ε_u with σ_y and n for a constitutive equation with $\kappa_{sh} = 17.6$ MPa and $\varepsilon_y = 0.002$.

maximum saturation level for σ_{sh} increases with decreasing temperature, but is reached only at higher strains. However, over the strain range which is experimentally limited by the onset of necking, the curves in Fig. 2(a) tend to overlap. As shown in Fig. 2(b), strain hardening in the V–4Cr–4Ti alloy (this example is at 25 °C) is qualitatively similar to that observed in the martensitic steels. However, in this case the hardening rate is lower by a factor of ≈10–15, very consistent with the large grain size in the recrystallized vanadium alloy.

These results indicate the critical microstructural feature controlling strain hardening in the unirradiated alloys examined in this study is the grain or subgrain dimension. Finer scale precipitate features play a role in σ_y but not $\sigma_{sh}(\varepsilon, T)$. Verification of the $\sigma_{sh}(\varepsilon, T)$ at higher strains is underway.

3. Effects of irradiation on e_u and the relation between $s(e)$ and $\sigma(\varepsilon)$

If strain hardening is represented by a simple power law term as $\sigma(\varepsilon) = \sigma_y + \kappa_{sh}(\varepsilon/\varepsilon_y)^n$, the necking instability at $\varepsilon_u = \ln(1 + e_u)$ occurs at the point where the load (P) for continued deformation peaks is given by the implicit expression [14]:

$$\varepsilon_u^{n-1} = [\varepsilon_y^n \sigma_y/\kappa_{sh} + \varepsilon_u^n]/n. \quad (2)$$

Thus ε_u is controlled not only by κ_{sh} and n, but also by σ_y. Increases in σ_y lead to a decrease in ε_u, even when κ_{sh} and N are constant. Eq. (2) is a completely general result, that differs from the normal simple power law stability criteria $e_u \approx n$. Thus the low values of e_u observed in irradiated alloys are consistent with a combination of reduced, but finite, strain hardening and large increases in σ_y. Flow localization is not a necessary controlling mechanism. This is illustrated in Fig. 3, which shows values of ε_u for $\kappa_{sh} = 17.6$ MPa, $\varepsilon_y = 0.002$, and varying n and σ_y. The filled circles illustrate a possible trajectory of irradiation induced decreases in n and increases in σ_y that produce a very large reduction in ε_u.

The simple necking instability analysis cannot model the post-necking $s(e)$ as needed provide information on $\sigma(\varepsilon)$ at high ε. Thus the ABAQUS FE code [18] was used to simulate tensile tests of flat dogbone-shaped tensile specimens with an initial length (L_0), width (W_0), and thickness (t_0) with ratios of 4:1:0.2 to relate the *extrinsic observable* $s(e)$ to a corresponding specified *intrinsic material* $\sigma(\varepsilon)$ that cannot be directly observed in a tensile test. Note it is important to emphasize that the $\sigma(\varepsilon)$ is an effective stress–strain relation, defined within the framework of J_2 incremental flow theory. Details of a large set of parametric simulations was used to gain a general insight on the effect of systematic variations $\sigma(\varepsilon)$ on the corresponding $s(e)$ are given elsewhere [14].

One example is shown in Fig. 4 for linear strain softening with $\sigma_y = 800$ and $\sigma(\varepsilon) = \sigma_y - C\varepsilon$ for C from 0 to 4000 MPa (Fig. 4(a)). As a consequence of immediate necking, e_u is ≈0 in all cases. True-strain softening effects are greatly amplified in the corresponding rate of drop-off in the $s(e)$ curve. Even a modest reduction in the magnitude of strain softening of 40 MPa at $\varepsilon = 0.01$ (only 5% of σ_y) leads to a large reduction of the engineering strain at $s_y/2$ to $e = 0.01$ compared to $e = 0.08$ for the perfectly plastic, $C = 0$ case (Fig. 4(b)). When compared with experimental $s(e)$ curves, these results place distinct limits on the rate and persistence of strain softening.

A $\sigma(\varepsilon)$ that provides a good approximation of a particular experimental $s(e)$ curve can be found based on the FE simulations by iteration. Fig. 4 shows $\sigma(\varepsilon)$ (Fig. 4(c)) fits to experimental $s(e)$ (dashed lines in Fig. 4(d)) for V–4Cr–4Ti alloy shown in Fig. 1 for both the 100 °C unirradiated (u) and 270 °C irradiated (i) conditions. The unirradiated $s_u(e)$ curve requires a $\sigma_u(\varepsilon)$ with a small low hardening Luders-type strain region, followed by significant strain hardening. In contrast, the $\sigma_i(\varepsilon)$ *that is required to be consistent with the experimental irradiated* $s_i(e)$, is characterized by a small initial increment of strain softening, followed by a modest strain hardening regime. A very notable result is that the irradiated $\sigma_i(\varepsilon)$ remains substantially higher than the corresponding $\sigma_u(\varepsilon)$ at all strains. That is, *irradiation hardening is persistent* and is only modestly decreased by high plastic strain. The dashed-dotted line in Fig. 4(c) shows a lower bound estimate of irradiation hardening $\Delta\sigma(\varepsilon) \approx \sigma_i(\varepsilon) - \sigma_u(\varepsilon)$, ignoring the difference in test temperature and assuming that the 'normal' strain hardening is not affected by irradiation. Even for these bounding assumptions, ≈70% of the initial irradiation hardening persists up to $\varepsilon = 0.4$.

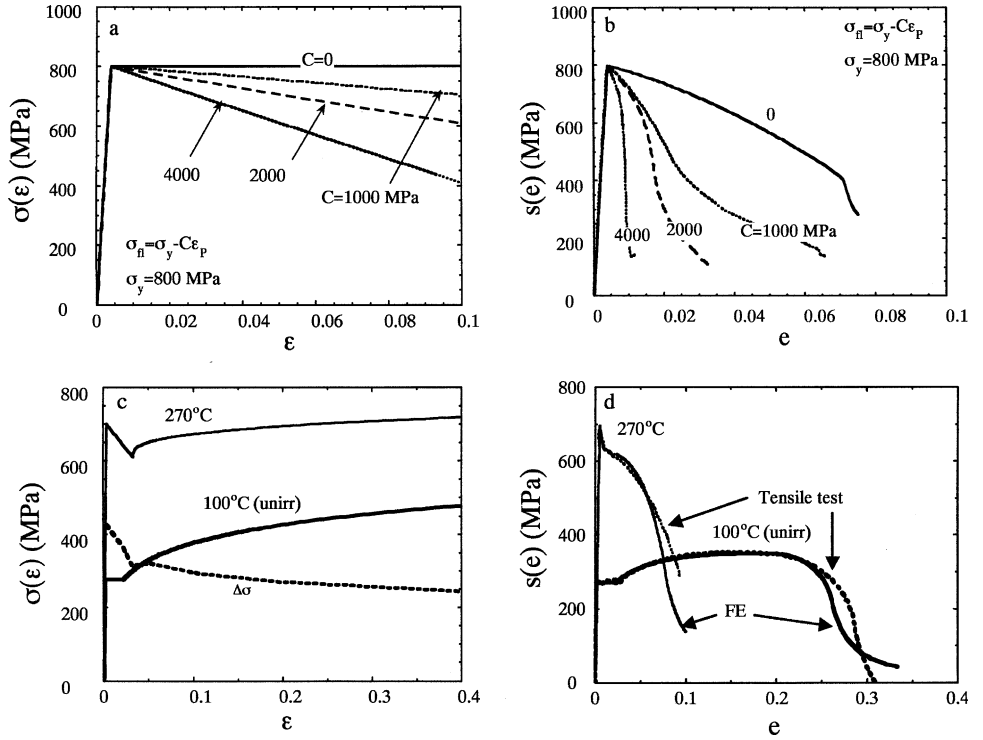

Fig. 4. (a) The $\sigma(\varepsilon)$ with systematic variation in the strain softening coefficient C; (b) the variation of calculated engineering stress–strain curves with increasing C. (c) The $\sigma(\varepsilon)$ that provide reasonable fits to the unirradiated (100 °C) and irradiated (270 °C) $s(e)$ curves, and the difference representing a lower bound estimate of the hardening due to irradiation as a function of ε; (d) the unirradiated and irradiated $s(e)$ curves corresponding to the $\sigma(\varepsilon)$ in Fig. 4(c).

4. Modeling of strain softening due to shear bands

As noted in the introduction, materials that undergo heterogeneous deformation, such as channeling, still must obey the basic continuum laws of solid mechanics. Thus we also investigated the interplay between the effects of spatially varying constitutive behavior. Specifically effective mesoscale continuum mechanics $\sigma(\varepsilon)$ were derived from FE simulations of strain softening shear bands $\sigma_{sb}(\varepsilon)$ that are embedded in a strain hardening matrix $\sigma_m(\varepsilon)$. The basic objective is to determine the composite material $\sigma(\varepsilon)$ as a function of the combined characteristics of the shear bands and matrix. Note this $\sigma(\varepsilon)$ differs from a true stress–strain constitutive law for a homogeneously deforming material, and provides a physically weighted average of the effects of the parameters describing the individual regions. While the computations themselves do not contain an absolute length, these results apply on a mesoscopic scale of the actual shear band dimensions. The overall composite $\sigma(\varepsilon)$ is controlled by the combination of parameters describing $\sigma_{sb}(\varepsilon)$ and $\sigma_m(\varepsilon)$, the geometry of the shear bands, the boundary conditions imposed on the computational cell and the general deformation stress-state. Baseline unit cell ABAQUS simulations were carried out as follows:

(1) The shear band zones were modeled as an elliptic zone in plane-strain in the larger transverse, width direction with free mirror boundary in the smaller transverse, thickness direction. The mirror condition ensures planar boundaries are maintained as the cell deforms. In contrast, use of periodic boundary conditions leads to shape changes in the cell. However, a direct comparisons showed that the $\sigma(\varepsilon)$ are generally similar for mirror and periodic boundaries. The plane-strain condition is one computable limit on the degree of constraint on the deformation. Another is plane-stress. While reality probably falls in between, the plane-strain condition is believed to be somewhat more applicable to shear bands in polycrystalline grains in the necking region of the specimen. Direct comparisons showed that at low ε the $\sigma(\varepsilon)$ for plane-stress is qualitatively similar to that for plane strain. However compared to plane-strain where initial softening is followed by re-hardening (see the plane strain results below), plain-stress conditions result in continual gradual strain softening beyond the initial drop. More detailed evaluations of cell boundary stress-state effects are underway and the results will be reported in future publications.

(2) The shear band geometry is characterized by orientation with respect to the tensile axis ($\theta = 0°$ to 45°)

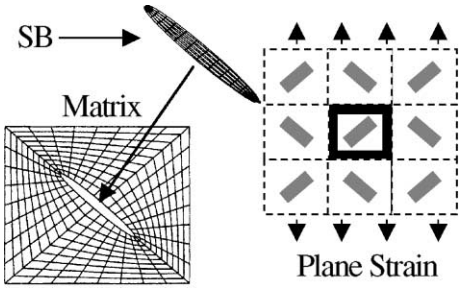

Fig. 5. FE mesh for the cell model of heterogeneous deformation.

and volume fraction (f_{sb}). The θ and f_{sb} also represent the mirror symmetry planes occupied by the shear bands and the extent which they approach a fully interconnected network.

(3) Separate local constitutive models are applied to the shear bands matrix: matrix – $\sigma_m(\varepsilon) = \sigma_y + C_m[(\varepsilon/0.0025)^n - 1]$ and shear band – $\sigma_{sb}(\varepsilon) = \sigma_y - C_{sb1}\varepsilon$ down to a minimum flow stress, σ_{sbm}; alternately we used $\sigma_{sb}(\varepsilon) = \sigma_y - C_{sb2} + C_{sb2}[\exp(-\varepsilon/\lambda)]^{1/2}$, where the σ_y, C_m, C_{sb1} and C_{sb2} characterize a specified combination of stress–strain laws for the two regions. Fig. 5 illustrates the cell model and structure of the ABAQUS FE mesh. A typical mesh has 384 eight-node biquadratic elements and 1243 nodes.

Fig. 6(a) and (b) show $\sigma(\varepsilon)$ for two f_{sb} of 0.025 and 0.05 along with $\theta = 45°$, $\sigma_y = C_m = 500$ MPa, $C_{sb1} = 1000$ MPa and $\sigma_{sbm} = 100$ MPa. There is a decrease in $\sigma(\varepsilon)$ after a small increment of hardening in both cases. The drop-off is larger and occurs at lower strains for $f_{sb} = 0.05$. The effect of a perfectly plastic shear band ($n = 0$) and shear band with $\sigma = 0$, or a hole, are also shown. Perfectly plastic shear bands have only a small effect on $\sigma(\varepsilon)$, while the hole reduces $\sigma(\varepsilon)$ by factors of $\approx$0.5 ($f_{sb} = 0.05$) to 0.75 ($f_{sb} = 0.025$). The minimum strength of a strain-softening shear band, $\sigma_{sbm} = 100$ MPa, keeps the $\sigma(\varepsilon)$ slightly above that for a hole. Fig. 6(c) shows the effect of increasing the shear band softening rate from 500 to 2000 MPa for f_{sb} of 0.025 with all other parameters fixed at the values in Fig. 6(a) and (b). Increasing C_{sb1} decreases the regime of hardening and increases the rate of drop-off in $\sigma(\varepsilon)$; however it does not influence the hardening region at high strain. Fig. 6(d)

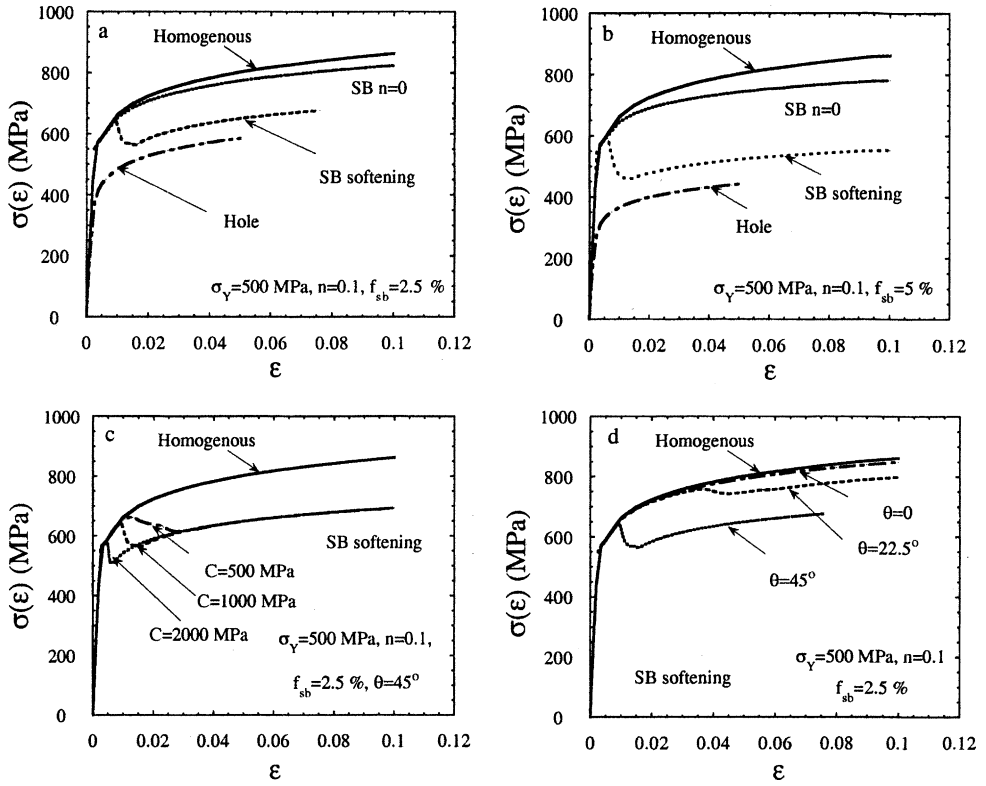

Fig. 6. (a) and (b) Stress–strain curves $\sigma(\varepsilon)$ obtained by the cell model for two f_{sb} of 0.025 and 0.05 for $\theta = 45°$, $\sigma_y = C_m = 500$ MPa, $C_{sb1} = 1000$ MPa and $\sigma_{sbm} = 100$ MPa; (c) the effect of increasing the shear band softening rate from 500 to 2000 MPa for f_{sb} of 0.025 with all other parameters fixed as in Fig. 6(a); (d) the effect of variations in θ of 0°, 22.5° and 45° for $C_{sb1} = 1000$ MPa and all other parameters fixed as in Fig. 6(a).

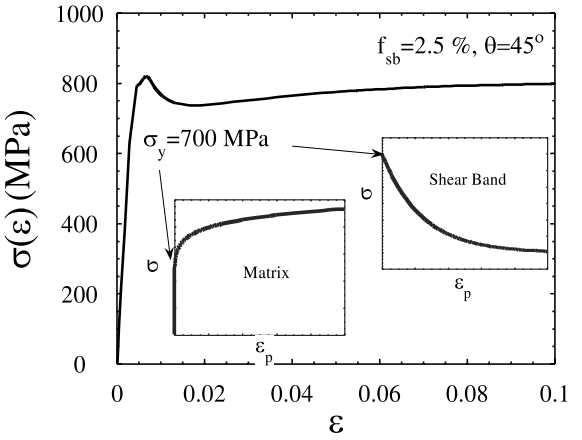

Fig. 7. Stress–strain curves $\sigma(\varepsilon)$ obtained for the cell model for $f_{sb} = 0.025$, $\sigma_y = 700$ MPa, $n = 0.1$, $\theta = 45°$, $C_{sb2} = 600$ MPa and $\lambda = 0.12$.

shows the effect of variations in θ of 0°, 22.5° and 45° for $C_{sb1} = 1000$ and all other parameters fixed as in Fig. 6(c). Compared to the 45° case, the effects of the shear bands are very small for $\theta = 0$ and much less for $\theta = 22.5°$.

Fig. 7 shows the result for a $f_{sb} = 0.025$, $\sigma_y = 700$ MPa, $n = 0.1$, $\theta = 45°$, $C_{sb2} = 600$ MPa and $\lambda = 0.12$. This $\sigma_{sb}(\varepsilon)$ model approximates the local strain dependent destruction of dislocation pinning features in a shear band. The resulting curve qualitatively resembles the $\sigma(\varepsilon)$ shown in Fig. 4(c) that is consistent with irradiated engineering $s(e)$ curve with $e_u \approx 0$ and an apparent yield drop shown in Fig. 4(d).

It is emphasized that these simulations primarily provide qualitative insight rather than a unique quantitative description of the underlying parameters that result in $\sigma(\varepsilon)$ characteristic of irradiated materials. Implications of this insight are discussed briefly below.

5. Discussion

The analysis presented in Sections 3 and 4 provide the first linkages between the micro and meso-scale phenomena of flow localization in irradiated alloys and the key macroscopic observable in a tensile test. Perhaps the most important result is given in Section 3, linking the intrinsic material $\sigma(\varepsilon)$ curve to extrinsic engineering $s(e)$ data. These FE simulations lead to several important conclusions: (1) the actual regime of strain softening is limited and gradual and is followed by strain hardening; and (2) standard plasticity models based on J_2 flow theory can be used, at least in some cases, like the tensile test, in FE simulations of deformation for finite geometry conditions; (3) radiation hardening persists up to high strains. Further, it is noted that the *apparent* yield drops of the type seen in Fig. 1 previously have been *qualitatively* interpreted to demonstrate a dislocation source hardening mechanism associated with unlocking dislocations from defect atmospheres. Further, the low uniform engineering strains have been qualitatively causally linked to localization of flow in narrow channels associated with strain induced destruction of hardening defects. However, both of these conceptual interpretations lack physical rigor and the more quantitative results presented in this work clearly demonstrate that neither hypothesis is necessary nor sufficient to explain the observables in a tensile test.

The analysis of the consequences of heterogeneous deformation in materials with strain softening shear bands presented in Section 4 represents an attempt to add some rigor to the analysis of deformation in irradiated metals and alloys. Note more detailed analysis of the FE results, including assessment of stress, strain and stress-state distributions as a function of the composite strain has been carried out, but cannot be described due to length limitations in this paper.

Space also does not permit a full discussion of the implications of the models to ongoing and future experiments. Indeed, while these results do not represent a final and comprehensive model, they provide considerable insight, particularly for guiding basic experimental observations. In summary, the empirical $\sigma(\varepsilon)$ for irradiated alloys are consistent with heterogeneous deformation in cases where the shear bands that become very soft with respect to the surrounding matrix, but only under limited and experimentally verifiable conditions. For example, in addition to clearing the bands of irradiation hardening defects it appears that processes like retardation of cross slip are important. Further, the shear bands are effective only if they form an array of roughly 45° segments that occupy roughly 50% of the set of interconnected shear band planes. Other tests against observation include mesoscopic strain distribution mapping, the types and variations in dislocation structures in the shear bands and matrix and the residual hardness in shear band and matrix regions at high strains.

It is necessary to obtain such information at high strains that are not accessible in simple tensile tests. However, we have compared the FE simulations to measured three-dimensional geometry changes in the evolving neck region of a tensile specimen. The excellent between the simulated and experimentally observed neck evolution supports the reliability and uniqueness of the $\sigma(\varepsilon)$ results derived by fitting the $s(e)$ data. Such comparisons are being extended to a variety of other test configurations, like indentations, compression and beam bending, that can more readily access high strains. Again, the key to the interpretation of such tests will be a direct comparison with FE simulations (analogous to that done for the tensile test in this paper) and well focussed links to observation.

Finally, we can only briefly note that the results in this study have very important practical implications with regard to the deformation limits in actual irradiated structures. Specifically deformation is controlled by an interacting combination of intrinsic and extrinsic factors. For example, deformation in compression would be expected to be more stable than in tension or shear dominated conditions.

6. Summary and conclusions

As noted in the introduction, a hierarchy of multiscale processes controls the engineering tensile stress–strain behavior, $s(e)$, of metals and alloys. Both the yield stress and strain hardening behavior can be modeled in terms of the underlying microstructure and microstructural evolution process associated with processing, irradiation service and deformation. Specifically, it is shown that strain hardening in unirradiated alloys can be treated on the basis of a competition between dislocation production and annihilation processes. Further, the key features of tensile test engineering $s(e)$ curves can be understood and modeled in terms of the corresponding continuum true stress–strain constitutive laws. The low e_u in tensile tests of irradiated alloys, reflects large increases in σ_y and reductions in strain hardening due to macroscopic necking that greatly amplifies the effects of more subtle changes in the high strain constitutive law.

We have specifically examined an extreme case of irradiated $s(e)$ curves, with negligible uniform strains, a pseudo yield drop, and continuous softening to failure at reduced total strains. The low uniform strains are due to continuum necking instabilities caused by *both* higher σ_y and reductions in the post-yield strain hardening. In this case the post-yield $\sigma(\varepsilon)$ shows an initial regime of modest strain softening over the first few percent of plastic strain, followed by a slight, but positive strain hardening. Lower bound estimates show substantial irradiation hardening persists up to high strains. Significantly, homogeneous constitutive models and J_2 incremental flow plasticity theory, used in large-scale deformation FE simulations, provide a useful engineering description of irradiated alloys. Further, macroscopic manifestations of irradiation effects on deformation can be represented by a continuum $\sigma(\varepsilon)$ in a way that is, at least in some cases, insensitive to details of the processes taking place on a finer scale, like flow localization.

A qualitative link between $\sigma(\varepsilon)$ and heterogeneous deformation is provided by a severely strain softening array of shear bands embedded in an irradiation and strain hardened matrix. Additional FE studies and analysis of the results will be combined with a wide array of experiments and observations to develop robust and fully quantitative deformation models.

Acknowledgements

This work was supported by the US Department of Energy Grant DE FG03-87-ER-52143. We also thank Steve Zinkle of ORNL for supplying the tensile data on irradiated and unirradiated V–4Ti–4Cr.

References

[1] P. Spätig, G.R. Odette, G.E. Lucas, J. Nucl. Mater. 275 (1999) 324.
[2] E.G. Donahue, G.R. Odette, G.E. Lucas, J. Nucl. Mater. 283–287 (2000) 637.
[3] P. Spätig, G.R. Odette, E. Donahue, G.E. Lucas, J. Nucl. Mater. 283–287 (2000) 721.
[4] A.F. Rowcliffe, J.P. Robertson, R.L. Klueh, K. Shiba, D.J. Alexander, M.L. Grossbeck, S. Jitsukawa, J. Nucl. Mater. 258–263 (1998) 1275.
[5] A.F. Rowcliffe, S.J. Zinkle, D.T. Hoelzer, J. Nucl. Mater. 283–287 (1998) 508.
[6] B.N. Singh, A.J.E. Foreman, H. Trinkaus, J. Nucl. Mater. 249 (1997) 103.
[7] N.M. Ghoniem, S.H. Tong, B.N. Singh, L.Z. Sun, Philos. Mag., in press.
[8] M. Victoria, N. Baluc, C. Bailat, Y. Dai, M.I. Luppo, R. Schäublin, B.N. Singh, J. Nucl. Mater. 276 (2000) 114.
[9] J.L. Brimhall, J.I. Cole, J.S. Vetrano, S.M. Bruemmer, Microstructure of irradiated materials, in: I.M. Robertson et al. (Eds.), MRS Symposium Proceedings 373, Materials Research Society, Pittsburgh, PA, 1995, pp. 177.
[10] H.M. Zbib, T. Diaz de la Rubia, M. Rhee, J.P. Hirth, J. Nucl. Mater. 276 (2000) 154.
[11] P.M. Rice, S.J. Zinkle, J. Nucl. Mater. 258–263 (1998) 1414.
[12] E.H. Lee, T.S. Byun, J.D. Hunn, N. Hashimoto, K. Farrell, J. Nucl. Mater. 281 (2000).
[13] Z.S. Basinski, M.S. Szczerba, J.D. Embury, Philos. Mag. A 76 (1997) 743.
[14] G.R. Odette, M.Y. He, E.G. Donahue, G.E. Lucas, On the relation between engineering load–displacement and true stress–strain behavior in tests of flat tensile specimens, in: M. Sokolov et al. (Eds.), Small Specimen Test Techniques-IV, ASTM SPT 1418, American Society for Testing and Materials, West Conshohocken, PA, in press.
[15] F.J. Zerilli, R.W. Armstrong, J. Appl. Phys. 61 (1987) 637.
[16] P. Spätig, R. Schäublin, M. Victoria, Material instabilities and patterning in metals, in: H.M. Zbib et al. (Eds.), MRS Symposium Proceedings, 683, 2001, BB1.10.1–BB1.10.6.
[17] P. Spätig, G.R. Odette, G.E. Lucas, M. Victoria, On the mechanical properties of the advanced martensitic steel EUROFER97, these Proceedings.
[18] ABAQUS V5.8, ABAQUS Standard Users Manual, Hibbitt, Karlsson and Sorenson, Inc., Providence, RI, 1998.